Deep-learning based three-dimensional label-free tracking and analysis of immunological synapses of chimeric antigen receptor T cells

Moosung Lee[a,b+], Young-Ho Lee[c+], Jinyeop Song [a,b+], Geon Kim[a,b], YoungJu Jo[a,b,d], HyunSeok Min[e], Chan Hyuk Kim[c*], and YongKeun Park[a,b,e*]

[a] Department of Physics, Korea Advanced Institute of Science and Technology (KAIST), Daejeon, South Korea

[b] KAIST Institute for Health Science and Technology, KAIST, Daejeon, South Korea

[c] Department of Biological Sciences, Korea Advanced Institute of Science and Technology, Daejeon, South Korea

[d] Present address: Department of Applied Physics, Stanford University, Stanford, CA 94305, USA

[e] Tomocube Inc., Daejeon, South Korea

+these authors contribute equally to this work.

*corresponding authors: C.H.K. (kimchanhyuk@kaist.ac.kr); Y.K.P (yk.park@kaist.ac.kr)

We propose and experimentally validate a label-free, volumetric, and automated assessment method of immunological synapse dynamics using a combinational approach of optical diffraction tomography and deep learning-based segmentation. The proposed approach enables automatic and quantitative spatiotemporal analyses of immunological synapse kinetics regarding morphological and biochemical parameters related to the total protein densities of immune cells, thus providing a new perspective for studies in immunology.

Understanding the immune response at cellular scales requires obtaining knowledge of interactions between immune cells and their microenvironment. One of the critical features for studying immunological activity is the immunological synapse (IS), a dynamically interacting junction between immune cells and their targets. Many hierarchical details related to the structural and signalling pathways activated during IS formation have been elucidated by fluorescence microscopic techniques, which have evolved from total internal reflection fluorescence microscopy for interfacial imaging[1] to light-sheet microscopy for volumetric imaging[2, 3]. Although such fluorescence-based techniques take a clear advantage of chemical specificity, they are also associated with innate limitations of photo-bleaching, photo-toxicity, and slow imaging, thereby necessitating the use of complementary label-free microscopy methods for evaluating single-cell dynamics[4]. Because the formations dynamics of IS occurs within a few minutes, rapid 4D imaging of immunes cells are required.

Here, we present a method for the systematic analysis of IS of immune cells. To track IS of live immune cells in a label-free and volumetric manner, three-dimensional (3D) refractive index (RI) tomograms of immune cells are measured using optical diffraction tomography (ODT), a 3D quantitative phase imaging technique[5]. In order to perform automated assessments of IS between immune and target cells, deep learning-based segmentation is employed to the 3D RI tomograms. To validate the method, we studied the IS formation dynamics of chimeric antigen receptor (CAR) T cells. 4D RI tomograms of CAR T cells and targets cells are measured at high speed (each tomogram measurement for every 3–5 seconds) for a long period of time (from 300 seconds to 10 minutes depending on cell types). The formation dynamics of IS of CAR T cells with various intrinsic functionalities are investigated. The dynamic formations of IS are systematically analysed by a deep-learning based automatic segmentation algorithm.

Methods

Optical Diffraction Tomography

In order to measure 3D RI tomograms of immune cells, an ODT setup (HT-2H, Tomocube Inc., Republic of Korea) was used. Based on the principle of inverse light scattering, ODT reconstructs 3D RI tomograms of transparent objects, from multiple 2D optical field images[6]. Due to its label-free and quantitative imaging capability, ODT has been used for the study of cell biology[7], hematology[8], hepatology[9], infectious diseases[10], and cytotoxicity[11].

The used setup is based on off-axis holograph equipped with a high-speed illumination scanner using a digital micro-mirror device (DMD) [12, 13]. A 2×2 single-mode fibre coupler was used to split a coherent, monochromatic laser ($\lambda = 532$ nm) into a sample and a reference arm, respectively. The DMD was then placed onto the sample plane of the sample arm to control the illumination angle of the first-order diffracted beam impinging onto a sample. To scan the illuminations at high angles, a 4-*f* array consisting of a tube lens ($f = 250$ mm) and a condenser objective (UPLASAPO 60XW, Olympus Inc., Japan) magnified the illumination angle. The light scattered by the samples was then transmitted through the other 4-*f* array formed by an objective lens (UPLASAPO 60XW, Olympus Inc., Japan) and a tube lens ($f = 175$ mm). The sample beam was combined with the reference beam by a beam splitter and filtered by a linear polariser. The resultant off-axis hologram was then recorded by an image sensor (FL3-U3-13Y3M-C, FLIR Systems, Inc., USA) that is synchronised with the DMD to record 49 holograms of the sample illuminated with different angles.

Using a phase-retrieval algorithm, the amplitude and phase images can be retrieved from the measured holograms. Based on the Fourier diffraction theorem with Rytov approximation[14, 15], the 3D RI tomogram of the sample was reconstructed from the retrieved amplitude and phase images. To fill up the uncollected side scattering signals due to the limited numerical apertures of objective lenses, the regularization algorithm based on the non-negative constrain was used[16]. The maximum theoretical resolutions of the ODT system were 110 nm laterally and 330 nm axially, according to the Lauer criterion[17]. Finally, the reconstructed RI values were converted into protein densities using the RI increment of $\alpha = 0.185$ ml/g[18, 19].

Segmentation algorithm

Dataset preparation using the watershed algorithm. To generate the ground truth masks of effector and target cells, we employed a watershed algorithm[20] according to the following steps. First, we processed a raw RI tomogram with four hyper-parameters: (1) initial seed locations for each cell, (2) RI threshold for defining cell boundaries, (3) voxel dilation sizes for merging over-segmented grains into one discrete region, and (4) standard deviation of the Gaussian smoothing mask. The processed tomogram was multiplied to a 3D distance-transform map of the cell regions and segmented by the watershed algorithm. Through iterative adjustment of the parameters, we obtained 236 pairs of 3D tomogram and segmentation masks for effector and target cells.

Automated segmentation strategy using deep learning. The requirement of iteration for parameter tuning of the watershed algorithm-based segmentation method to obtain a single well-segmented label is prohibitive for obtaining a dynamic dataset. Therefore, we employed a deep-learning approach to enable general, high-throughput, and automated segmentation for 3D tomograms. The deep neural network was designed with the main goal of regressing the distance map rather than classifying voxel-wise labels[21], regarding the following difficulties of our segmentation tasks: (1) indistinct boundaries between effector–target cell pairs in RI distributions, (2) diverse morphology of cells, and (3) demand for precise segmentation at high resolution. For our training purposes, we converted each label of effector and target cells into distance maps using Euclidean distance transformation, whereas we set the background to zero. Moreover, the effector and target cells were distinguished by their signs on the distance maps (i.e., positive and negative, respectively). The input and output data were 3D RI tomograms and estimated signed distance maps, respectively, with a dimension of $128 \times 128 \times 64$. During the inference, the output distance maps from the network were converted to segmentation masks through simple thresholding. Adopting distance regression improves segmentation accuracy and robustness to overfitting.

Network architectures. As shown in Supplementary Figure 1, the architecture of our network is based on a 3D UNet-like architecture, with proven good performance for biomedical segmentations[22]. The architecture is composed of a series of contracting and expanding paths; the former includes a series of residual blocks and down-pooling layers, and the latter involves a series of boundary refiners (BRs) and up-pooling layers. The number of filters for the five layers are [32, 64, 128, 128, 256]. The feature skip connection of our network passes through the global convolutional network[23], which was employed to increase the receptive field. Such modifications allowed the network to learn more about the overall cell morphology and critical characteristics of immune cells.

Training protocol. We divided the 236 curated training datasets into 198 training and 38 validation sets, respectively. We chose the L2 loss function setting, which is appropriate for a distance regression scheme. The model was trained with the Adam optimizer ($\alpha = 0.5$, $\beta = 0.99$) using a decaying learning rate (initial value = 0.001). For efficient training, we augmented the data using rotations, resizing, and elastic deformations. The network was trained on four graphics processing units (GPUs; GEFORCE GTX 1080 Ti) for 400 epochs, which took approximately 6 hours. Selection of a model for inference among trained models was based on performance on the validation set. Our network was implemented in Python using the PyTorch package (http://pytorch.org), and the other processing steps were performed in MATLAB.

Cell preparation and establishment of cell lines

Cell lines and culture. The K562 and K562-CD19 cell lines were kindly provided by Travis S. Young (California Institute for Biomedical Research), and cultured in RPMI-1640 medium supplemented with 10% heat-inactivated foetal bovine serum (FBS), 2 mM L-glutamine, and 1% penicillin/streptomycin in a humidified incubator with 5% CO_2 at 37°C. The Lenti-X™ 293T cell line was purchased from Takara Bio, which was maintained in Dulbecco's modified Eagle medium supplemented with 10% heat-inactivated FBS, 2 mM L-glutamine, 0.1 mM non-essential amino acids, 1 mM sodium pyruvate, and 1% penicillin/streptomycin.

Generation of K562-CD19-PD-L1 cells. To generate the $CD19^+PD\text{-}L1^+$ K562 cell line, the human *PD-L1* open reading frame (NM_014143.3) was inserted into the BamHI and SalI sites of pLV vectors (pLV-hPD-L1), and then 1×10^6 K562-CD19 cells were transduced with the lentiviral supernatant. Following transduction, PD-L1 expression was

analysed with an APC-conjugated anti-PD-L1 antibody (Cat # 329707, Biolegend) to select cells representing enrichment of a uniform PD-L1+ population.

Plasmid construction. Synthesis of CD19-specific chimeric antigen receptor (CD19-BBz CAR), which is composed of anti-CD19 scFv (FMC63) connected to a CD8α spacer domain and CD8α transmembrane domain, and the co-stimulatory domains of 4-1BB (CD137) and signalling domain of CD3ζ, has been previously described[24]. To enrich a uniform CAR-expressing T cell population, the cytoplasmic domain truncated *CD271* (ΔLNGFR) gene was amplified from pMACS-ΔLNGFR (Miltenyi Biotec., Germany) and overlapped with the oligonucleotide of P2A. This PCR product was overlapped with that of CD19-BBz CAR and then inserted into the BamHI and SalI sites of pLV vectors (pLV- ΔLNGFR-CD19-BBz CAR). For generation of PD-1-disrupted CD19-specific CAR-T cells, a short hairpin RNA (shRNA)-expressing cassette, composed of a mouse U6 Pol III promoter and a *PD-1* or *GFP* shRNA sequence 5′GCCTGTGGTTCTATTATATTATTTCAAGAGAATAATATAATAGAACCACAGGTTTTTG3′ and 5′CTCTCGGCATGGACGAGCTGTATTCAAGAGATACAGCTCGTCCATGCCGAGATTTTTG3′, respectively), was synthesised and sub-cloned into the HpaI site of pLV-ΔLNGFR-CD19-BBz CAR (pLV- ΔLNGFR-sh*GFP*/BBz-CAR or pLV- ΔLNGFR-sh*PD-1*/BBz-CAR).

To define the IS of CAR-T cells, we generated an mCherry-tagged CD19-BBz CAR construct. The mCherry gene was amplified from pLV-EF1a-MCS-IRES-RFP-Puro (Biosettia, USA), and overlapped with synthetic oligonucleotides of a G4S linker. This PCR product was then overlapped with that of CD19-BBz CAR and inserted into the BamHI and SalI sites of pLV vectors (pLV-BBz-CAR-mCherry).

Generation of CAR-transduced human T cells. To generate a recombinant lentivirus supernatant, 6×10^5 Lenti-X™ 293T cells were cultured in a six-well plate for 24 hours and transfected with the lentivirus packaging vectors (pMDL, pRev, pMDG.1) and the pLV vectors encoding ΔLNGFR-CD19-BBz CAR, ΔLNGFR-shPD-1/BBz-CAR, ΔLNGFR-shGFP/BBz-CAR, or BBz-CAR-mCherry using 10 μL of Lipofectamine 2000 reagent (Thermo Fisher). Two days after transfection, the lentivirus-containing supernatant was collected and stored at −80°C until use.

Peripheral blood mononuclear cells (PBMCs) were separated from whole blood samples of healthy donors using SepMate™ tubes (STEMCELL Technologies, Canada) following the manufacturer's instructions. The PBMCs were stimulated with 4 μg/mL of plate-bound anti-CD3 antibody (clone OKT3; Bio X cell), 2 μg/mL of soluble anti-CD28 antibody (clone CD28.2; Bio X cell), and 300 IU/mL human recombinant IL-2 (BMIKOREA).

Two days after stimulation, activated T cells were mixed with the lentivirus supernatant, centrifuged at 1000 ×*g* for 1 hour and 30 minutes, and incubated overnight at 37°C. CAR-transduced T cells were cultured at 1×10^6 cells/mL in RPMI-1640 medium supplemented with 10% heat-inactivated FBS, 2 mM L-glutamine, 0.1 mM non-essential amino acids, 1 mM sodium pyruvate, and 55 μM β–mercaptoethanol in the presence of human recombinant (rh)IL-2 (300 IU/mL) until sorting of CART19 cells from bulk T cells.

Flow cytometry. The expression level of anti-CD19 CAR was evaluated by biotin-conjugated rhCD19-Fc (Cat # CD9-H5259, ACRO Biosystems) with AF647-conjugated streptavidin (Cat # 405237, Biolegend). ΔLNGFR was detected by FITC-conjugated anti-CD271 antibody (Cat# 130-112-605, Miltenyi Biotec). The expression level of PD-1 in re-stimulated CART19 cells co-cultured with K562-CD19 cells for 3 days was measured by PE-conjugated anti-PD-1 antibody (Cat# 12-2799-42, Thermo Fisher).

Isolation of CAR-transduced T cells. Four days after transduction, ΔLNGFR-positive CART19 cells were isolated with the human CD271 MicroBead kit (Cat# 130-099-023, Miltenyi Biotec) following the manufacturer's instructions. Sorted CART19 cells were expanded for 6 days with RPMI-1640 medium supplemented with 10% heat-inactivated FBS, 2 mM L-glutamine, 0.1 mM non-essential amino acids, 1 mM sodium pyruvate, and 55 μM β–mercaptoethanol in the presence of rhIL-2 (300 IU/mL). For isolation of $CD4^+$ or $CD8^+$ CART19 cells, $\Delta LNGFR^+$ sh*GFP*/CART19 or $\Delta LNGFR^+$ sh*PD-1*/CART19 cells were stained with FITC-conjugated anti-CD4 (Cat# 11-0048-41, Thermo Fisher) and PerCP-Cy5.5-conjugated anti-CD8 antibody (Cat# 344710, Biolegend). $CD4^+$ or $CD8^+$ CART19 cells were sorted using the MoFlo Astrios sorter (Beckman Coulter). The flow cytometry-based isolation procedure resulted in a purity up to 98%.

Proliferation assay. Sorted $\Delta LNGFR^+$ sh*GFP*/CART19 cells or $\Delta LNGFR^+$ sh*PD-1*/CART19 cells (1×10^5) were cultured with γ-irradiated K562-CD19-PD-L1 cells (1×10^5) in a 24-well plate without exogenous cytokines. The fold-expansion of CAR-T cells was calculated by cell counting at day 6, 9, and 12 using trypan blue exclusion.

In vitro *cytotoxicity of CART19 cells.* K562-CD19-PD-L1 or K562-CD19 cells (5×10^6) were labelled with 2 μM CellVue® Claret Far-Red Fluorescent dye (Sigma-Aldrich). $LNGFR^+$ CAR-T cells were co-cultured with ClaretRed

labelled K562-CD19-PDL1 or K562-CD19 cells at a 1:1, 0.3:1, or 0.1:1 E:T ratio in a 24-well plate. Seventy-two hours after co-culture, 7-AAD was added to each well for detection of dead cells. The cytotoxic activity (%) of CAR-T cells was determined by flow cytometry, calculated by the formula $100 \times [1 - (\text{ClaretRed}^{+}\text{7-AAD}^{-}\ \%/\text{ClaretRed}^{+}\ \%]$.

Statistical Analysis

Sample means between two groups were calculated with the Mann-Whitney-Wilcoxon rank tests (Fig. 3 and Supplementary Fig. 8c–e or two-tailed Student t-tests (other supplementary figures). Significance among multiple groups was assessed with N-way analysis of variance (Table 1, Supplementary Figs. 7a and 8b). Data are presented as mean ± standard deviations.

Results and Discussions

Deep-learning-assisted segmentation of immunological synapse in label-free ODT

Based on ODT and deep-learning-based segmentation, we performed the 4D label-free tracking of IS dynamics (Fig. 1). Our ODT setup is equipped with a DMD as an illumination-scanning device, which enables the high-speed acquisition of a single tomogram within only 500 milliseconds (Fig. 1a, also see Methods). The 3D tomograms of cells convey information related with their RI values and corresponding total protein density distributions (Fig. 1b, also see Methods). To define the D IS areas between interacting cells, we developed an automatic 3D cell segmentation approach based on deep-learning techniques (see Methods). The main component of our segmentation strategy, the UNet-like deep neural network[22], was trained using our processed dataset (Supplementary Fig. 1). The dataset consisted of 236 tomograms and segmentation labels were obtained from the watershed algorithm, one of conventional methods for cell segmentation (see Methods)[20]. Use of the watershed algorithm alone requires a laborious iteration of parameter tunings to obtain a single well-segmented label, whereas the deep-learning segmentation strategy enabled conducting a general, high-throughput, and automated analysis of cell dynamics.

Because our label-free segmentation approach aims to distinguish the boundaries between two attached cells at a sub-micrometre spatial resolution, it was first essential to validate whether this segmentation accuracy is sufficient for this purpose. To address this question, we compared the segmentation performances between the watershed-based segmentation and our deep-learning-based segmentation approaches (Supplementary Figs. 2–3). A qualitative comparison showed that our model could successfully define IS boundaries without ill-defined segmentations. Interestingly, our model showed better segmentation performances than the watershed algorithm overall (Supplementary Fig. 2). Moreover, quantitative comparison based on 3D intersection-over-union and mean-displacement-error with fluorescence-based labels showed that our model outperformed the watershed-based segmentation performances for IS, even for untrained datasets (Supplementary Fig. 3). We further confirmed that the general, high-throughput segmentation capability exceeded a field-of-view of 1 mm^2 (Fig. 1c). These validations led us to conclude that our deep-learning model could be generally utilised throughout 4D IS analyses with high fidelity.

Tracking initial IS formation dynamics of CAR-T cells

We then applied this method to study the IS formation dynamics of CD19-positive K562 cells and CD19-specific chimeric antigen receptor (CART19) T cells, which have attracted interest in the field of immuno-oncology owing to their potential as next-generation anticancer drug targets[25, 26]. Chimeric antigen receptor (CAR) is a fusion protein composed of targeting, hinge, transmembrane, and intracellular signalling domains that can bind to targets in a different manner from observed for T cell receptor (TCR)[27]. Whereas TCR recognises peptide-loaded major histocompatibility complex (pMHC), CAR recognises surface proteins through targeting domains composed of single-chain variable fragments (scFv) derived from an antibody. Although CAR/antigen and TCR/pMHC complexes have different IS structures[6], the majority of studies on IS dynamics have focused on the influence of the TCR/pMHC complex, with minimal information available for the dynamics driven by the CAR/antigen complex.

Thus, to better understand these CAR/antigen-mediated IS dynamics, we utilised our method to investigate the signalling-dependent IS formation between CART19 (effector) cells and K562-CD19 (target) cells (Supplementary Fig. 4). Specifically, we examined the dynamics of IS formation depending on the presence of CD19 on target cells (Fig. 2, see Methods). In the absence of CD19 expression on target cells (K562), CART19 cells could not form a stable synapse in five independent experimental trials (Fig. 2a, Supplementary Video 1). By contrast, CART19 cells formed a stable IS with CD19-positive K562 (K562-CD19) cells after the first contact, and induced blebs on the target cell (Fig. 2b, Supplementary Video 2).

The initial IS formation dynamics between CART19 cells and K562-CD19 cells exhibited three common kinetic behaviours. First, the synapse areas reached a steady state within only 3 minutes. Second, protein density maps indicated polarisation of the intracellular organelles in CART19 cells until stabilisation, which is similar to the polarisation of cytotoxic T lymphocytes stimulated by TCRs[2]. Third, the surface protein densities of CART19 cells on IS were higher

than those observed on the non-contact T surfaces of CART19 cells, which is consistent with a recent observation that the IS incorporates larger amounts of proteins, including CARs, actins, and other antigen clusters[28].

We then quantitatively analysed the aforementioned dynamic behaviours in the initial IS formation stage (Figs 2c–e). Analysis of the initial synapse area changes over time showed marked differences in the curves for K562-CD19 and K562 cells, clearly indicating a mechanism of CD19-dependent synapse stabilisation (Fig. 2c). To determine the saturation kinetics of IS formation between CART19 and K562-CD19 cells, we fitted a temporal mean synapse area graph with a rational curve. We also investigated the mechanical dynamics of CART19 cells during initial IS stabilisation by plotting the temporal movement of CART19 cells with a rational curve (Fig. 2d). Comparison of the half-lives ($\tau_{1/2}$; time for the value to reach the half maximum value) showed that the cell displacement was prolonged compared to the time required for stabilization of IS areas, which is attributed to the mechanical actions that T cells act exert on their target during IS formation and the subsequent translational and rotational displacements[29] (Supplementary Video 3).

To quantify the surface protein densities on IS, we compared the temporal changes in the mean surface protein densities of IS and the non-contact T surface (Fig. 2e). As shown in Fig. 2b, IS had rapidly increasing surface protein densities reaching up to 0.027 pg/μm^2 at 300 seconds, whereas the non-contact T surface was maintained at 0.019 pg/μm^2.

Statistical analyses of IS-related morphological parameters

Having established that initial CART19 IS kinetics rapidly reach a steady state, we next evaluated whether these stabilised synapses exhibit any morphologically distinct property depending on the intrinsic functionalities of CART19 cells. We statistically compared the dependence of IS areas on CART19 functionalities categorised into (i) resting and re-stimulated states, (ii) $CD4^+$ and $CD8^+$ subtypes, and (iii) PD-1 wild-type (WT) and PD-1 knockdown (KD) states (see Methods, Supplementary Figs. 5–6). Because IS areas may be affected by the sizes of activated cells, we also compared the dry masses and synapse area portions (IS areas divided by total CART19 surface areas).

Multi-way analysis of variance indicated that the activation status of CART19 cells strongly affects most of the parameters evaluated (Table 1). Interestingly, both $CD4^+$/$CD8^+$ subtypes and PD-1 expression levels also significantly affected both the dry masses and IS parameters. To examine the correlations between CART19 functions and morphological parameters in detail, we further analysed the statistics of dry masses and IS parameters for each group separately (Fig. 3). The re-stimulated CART19 cells had greater dry masses than resting CART19 cells (Fig. 3a), and the dry masses significantly differed among subtypes of CART19 cells. In resting states, $CD8^+$ CART19 cells showed larger mean values than $CD4^+$ CART19 cells, whereas $CD4^+$ CART19 cells were heavier after re-stimulation. The PD-1 KD in CART19 cells did not significantly affect dry mass changes, indicating that the sizes of activated CART19 cells more strongly depend on T subtypes than on intrinsic PD-1 expression levels. Moreover, the PD-1 KD in re-stimulated $CD8^+$ CART19 cells significantly decreased IS areas (Figs. 3b-c). The decrease of IS area was independent of the PD-L1 expression level on K562 cells, although the PD-1 KD in CAR-T cells enhanced the long-term cytotoxicity and proliferation of CART19 cells with K562-CD19-PD-L1 cells (Supplementary Figs. 7-8).

Summary

Our statistical analyses suggest that PD-1/PD-L1 interactions do not significantly contribute to the initial IS morphology, although the PD-1/PD-L1 axis plays roles in the inhibition of long-term cytotoxic and proliferative signalling pathways. This appears to conflict with a previous observation that the initial clustering of TCRs depends on PD-1/PD-L1 checkpoint signalling[30]. Therefore, it is necessary to further clarify the mechanism by which intrinsic CAR functionalities play a significant role in initial IS morphology and whether the different IS mechanism of CARs and TCRs may explain the different PD-1/PD-L1 interactions occurring during initial IS formation.

In summary, we combined ODT and a deep learning-based segmentation strategy to successfully realize label-free 4D IS tracking. The present proof-of-concept focused on the initial IS formation dynamics of CART19 cells, but the proposed method can be generalised to studying a broad range of immunological phenomena from TCR signalling pathways to the cytotoxicity of innate immune cells. We anticipate that the combination of correlative imaging with fluorescence microscopy will improve the precision and accuracy of our proposed method, and provide the chemical specificities required to fully elucidate the IS formation mechanisms[31, 32, 33].

METHODS

Supplementary Information and Source Data files are available in the online version of the paper.

ACKNOWLEDGEMENTS

This work was supported by KAIST, Tomocube, National Research Foundation of Korea (NRF) (2017M3C1A3013923, 2015R1A3A2066550, 2018K000396, 2018R1A6A3A01011043), the Bio & Medical Technology Development Program of NRF funded by the Ministry of Science & ICT (2014M3A9D8032525), KAIST GCORE(Global Center for Open Research with Enterprise) grant funded by the Ministry of Science and ICT (N11190028).

AUTHOR CONTRIBUTIONS

Y.-K.P. and C.-H.K. initiated the work and supervised the project. M.L. and Y.-H.L. performed the experiments. M.L. and J.S. developed the methods. All authors wrote the manuscript.

COMPETING FINANCIAL INTERESTS

Prof. Park and Mr. M. Lee have financial interests in Tomocube Inc., a company that commercialises optical diffraction tomography and quantitative phase-imaging instruments, and is one of the sponsors of the work.

Figures

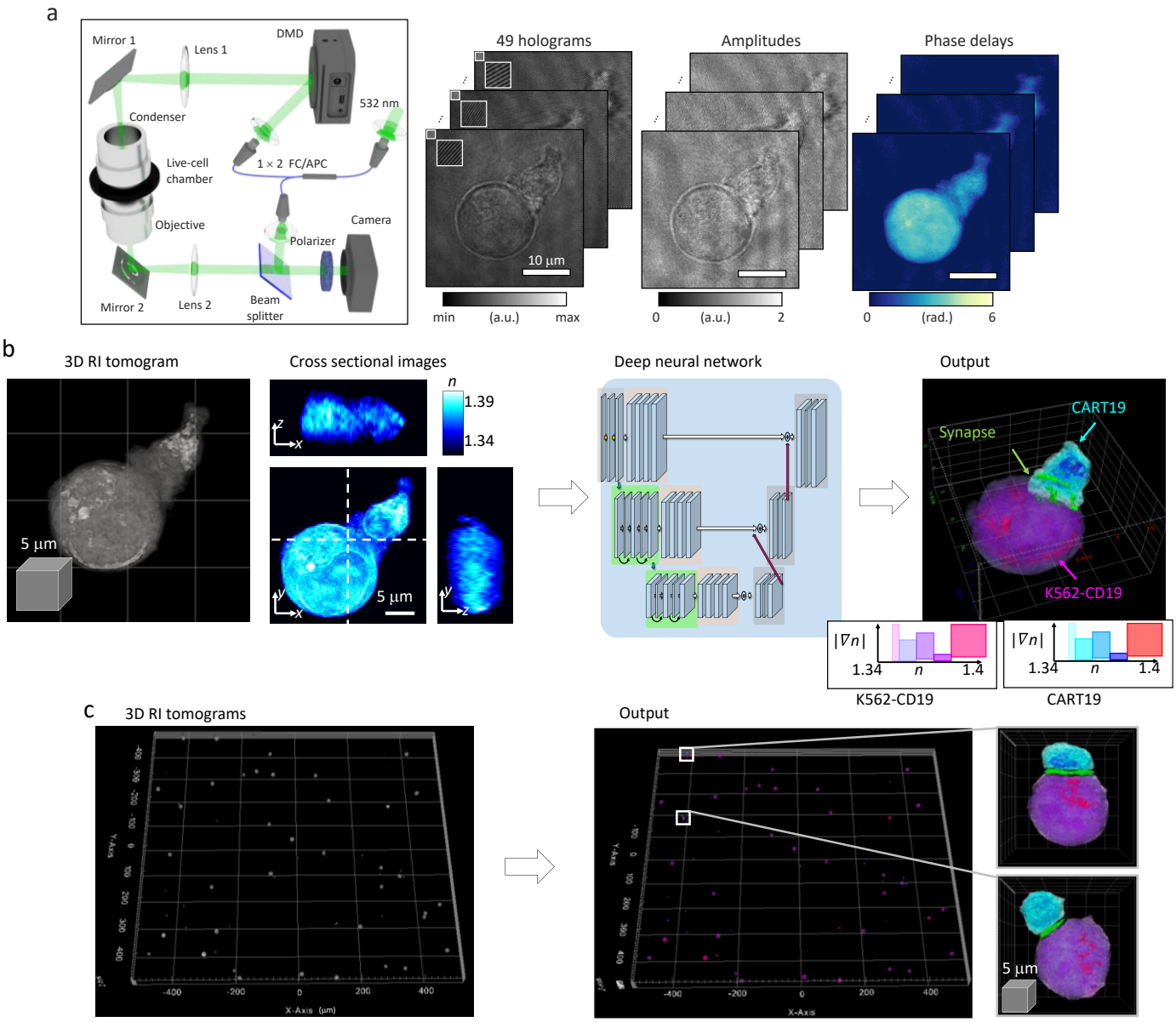

Figure 1 Flow chart of label-free synapse reconstruction. (a) Data acquisition in optical diffraction tomography (ODT). The experimental setup for ODT is based on a digital micro-mirror device (DMD) for high-speed illumination scanning. Forty-nine holograms at various illumination angles were recorded, and their amplitude and phase delay distributions were retrieved. **(b)** Synapse reconstruction. A reconstructed refractive index (RI) map (left) was used as an input for our deep-learning model. The model segments CART19 and K562-CD19 cells and defines the immunological synapse. Colour maps are based on the two-dimensional ranges of RI and the RI gradient. **(c)** High-throughput segmentation over 0.98 × 1.05 × 0.04 mm^3. Representative effector–target cell pairs are magnified on the right.

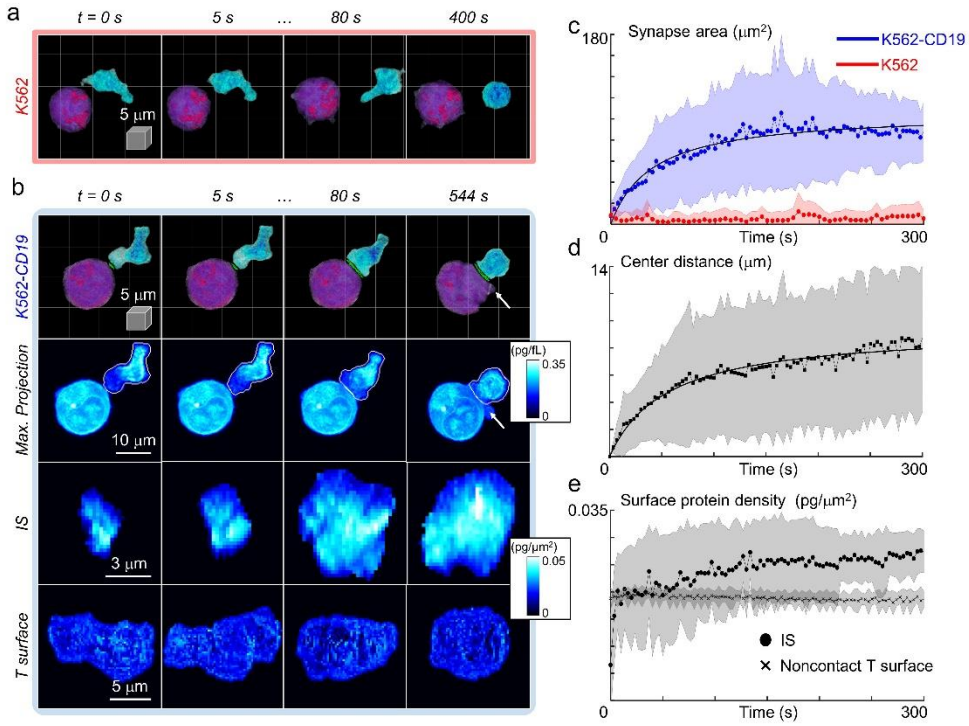

Figure 2. Quantification of initial synapse formation kinetics of CAR-T cells. (a) Representative still images of a time-lapse video of CART19 cells (blue) responding to K562 cells (purple): 0 seconds indicates the initial contact time of an effector cell and a target cell. **(b)** Representative still images of a time-lapse video of CART19 cells responding to K562-CD19 cells. First row: Green areas indicate immunological synapses (IS). The white arrow indicates a bleb. Second row: Maximum projection of 3D protein density distributions along the z direction. Third row: Maximum projection of surface protein density of IS. Fourth row: Maximum projection of surface protein density of the non-contact T surface. **(c)** Temporal changes in the mean synapse areas of CART19 cells responding to K562 cells (n = 5) and K562-CD19 cells (n = 22). Black line: fitting curve with $A(t) = 106.16t/(t + 39.63)$, Pearson correlation coefficient = 0.93. Dots and shading at each point indicate the mean and standard deviation, respectively. **(d)** Temporal changes in the mean displacements of the centre-of-volume of CART19 cells responding to K562-CD19 cells. Black line: fitting curve with $d(t) = 9.38t/(t + 55.16)$, Pearson correlation coefficient = 0.96. **(e)** Temporal changes in the mean surface protein densities of CART19 immunological synapses (circles) and non-contact T surfaces (crosses) responding to K562-CD19 cells. The mean surface protein densities of IS and non-contact T surface at 300 seconds were 0.027 ± 0.004 and 0.019 ± 0.001 pg/μm^2, respectively.

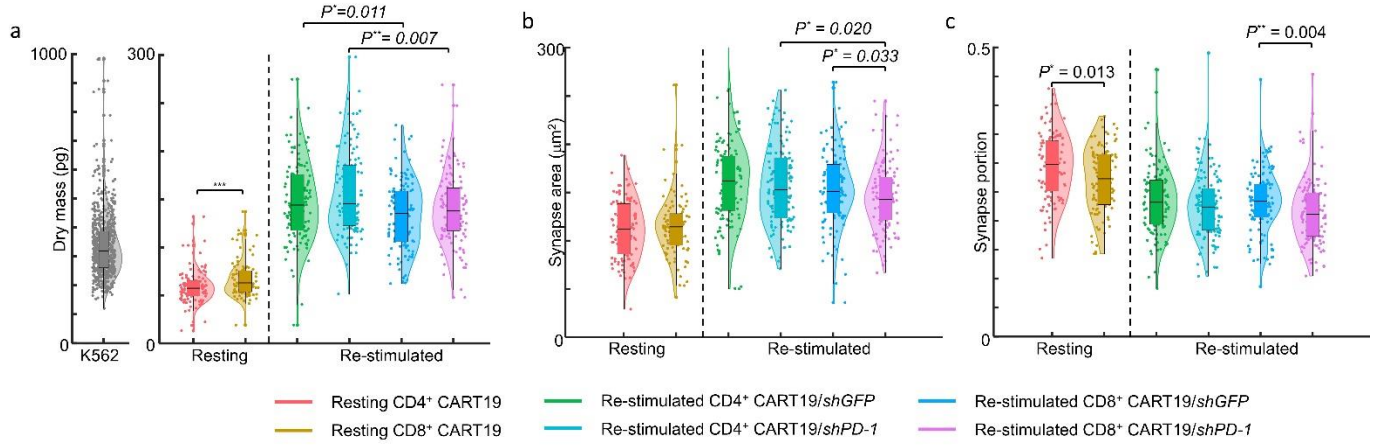

Figure 3. Statistical analyses of synapse morphologies depending on the cell-intrinsic functions of CART. (a) Scatterplots of dry masses. **(b) (c)** Scatterplots of synapse area-per-surface areas Each boxplot indicates the median, upper, and lower quartiles of each population. The attached lines indicate the range of the population. Perpendicular shades indicate the normalized population density distributions. $^{*}p < 0.05$, $^{**}p < 0.01$, $^{***}p < 0.001$ by two-tailed Wilcoxon tests. mean ± SD data are available in Supplementary Table 1.

P value *F value*	Dry mass	Synapse area	$\frac{\text{synapse area}}{\text{surface area}}$
Resting/ Re-stimulated	< 0.001	< 0.001	< 0.001
	543.84	158.74	80.92
$CD4^+$/ $CD8^+$	0.002	0.028	0.013
	9.88	4.84	6.2
shGFP/ shPD-1	0.013	0.072	0.016
	6.19	3.25	5.87

Table 1. Multi-way analysis of variance (P-values and F-values) for (1) dry mass, (2) synapse area, and (3) synapse area portion depending on (i) resting and re-stimulated states, (ii) $CD4^+$ and $CD8^+$ subtypes, and (iii) PD-1 wild-type (WT) and PD-1 knockdown (KD) states.

References

1. Grakoui A, *et al.* The immunological synapse: a molecular machine controlling T cell activation. *Science* **285**, 221-227 (1999).

2. Ritter AT, *et al.* Actin depletion initiates events leading to granule secretion at the immunological synapse. *Immunity* **42**, 864-876 (2015).

3. Chen B-C, *et al.* Lattice light-sheet microscopy: Imaging molecules to embryos at high spatiotemporal resolution. *Science* **346**, 1257998 (2014).

4. Skylaki S, Hilsenbeck O, Schroeder T. Challenges in long-term imaging and quantification of single-cell dynamics. *Nat Biotechnol* **34**, 1137-1144 (2016).

5. Park Y, Depeursinge C, Popescu GJNP. Quantitative phase imaging in biomedicine. **12**, 578 (2018).

6. Kim K, *et al.* Optical diffraction tomography techniques for the study of cell pathophysiology. **2**, (2016).

7. Kim T-K, *et al.* Physicochemical Properties of Chromosomes in Live Cells Characterized by Label-Free Imaging and Fluorescence Correlation Spectroscopy. 533596 (2019).

8. Kim Y, Shim H, Kim K, Park H, Jang S, Park YJSr. Profiling individual human red blood cells using common-path diffraction optical tomography. **4**, 6659 (2014).

9. Kim K, Lee S, Yoon J, Heo J, Choi C, Park YJSr. Three-dimensional label-free imaging and quantification of lipid droplets in live hepatocytes. **6**, 36815 (2016).

10. Tougan T, *et al.* Molecular Camouflage of Plasmodium falciparum Merozoites by Binding of Host Vitronectin to P47 Fragment of SERA5. **8**, 5052 (2018).

11. Kwon S, *et al.* Mitochondria-targeting indolizino [3, 2-c] quinolines as novel class of photosensitizers for photodynamic anticancer activity. **148**, 116-127 (2018).

12. Shin S, Kim K, Yoon J, Park Y. Active illumination using a digital micromirror device for quantitative phase imaging. *Opt Lett* **40**, 5407-5410 (2015).

13. Lee K, Kim K, Kim G, Shin S, Park Y. Time-multiplexed structured illumination using a DMD for optical diffraction tomography. *Opt Lett* **42**, 999-1002 (2017).

14. Wolf E. Three-dimensional structure determination of semi-transparent objects from holographic data. *Optics Communications* **1**, 153-156 (1969).

15. Devaney AJ. Inverse-scattering theory within the Rytov approximation. *Opt Lett* **6**, 374-376 (1981).

16. Lim J, *et al.* Comparative study of iterative reconstruction algorithms for missing cone problems in optical diffraction tomography. **23**, 16933-16948 (2015).

17. Lauer V. New approach to optical diffraction tomography yielding a vector equation of diffraction tomography and a novel tomographic microscope. **205**, 165-176 (2002).

18. Barer R, Ross KF, Tkaczyk S. Refractometry of living cells. *Nature* **171**, 720-724 (1953).

19. Popescu G, *et al.* Optical imaging of cell mass and growth dynamics. **295**, C538-C544 (2008).

20. Meyer F. Topographic Distance and Watershed Lines. *Signal Process* **38**, 113-125 (1994).

21. Wang W, *et al.* Learn to segment single cells with deep distance estimator and deep cell detector. *eprint arXiv:180310829*, arXiv:1803.10829 (2018).

22. Ronneberger O, Fischer P, Brox T. U-Net: Convolutional Networks for Biomedical Image Segmentation. In: *Medical Image Computing and Computer-Assisted Intervention – MICCAI 2015* (ed^(eds Navab N, Hornegger J, Wells WM, Frangi AF). Springer International Publishing (2015).

23. Peng C, Zhang X, Yu G, Luo G, Sun J. Large Kernel Matters — Improve Semantic Segmentation by Global Convolutional Network. In: *2017 IEEE Conference on Computer Vision and Pattern Recognition (CVPR)* (ed^(eds) (2017).

24. Rodgers DT, *et al.* Switch-mediated activation and retargeting of CAR-T cells for B-cell malignancies. *Proceedings of the National Academy of Sciences* **113**, E459 (2016).

25. Porter DL, Levine BL, Kalos M, Bagg A, June CH. Chimeric antigen receptor-modified T cells in chronic lymphoid leukemia. *N Engl J Med* **365**, 725-733 (2011).

26. van der Stegen SJ, Hamieh M, Sadelain M. The pharmacology of second-generation chimeric antigen receptors. *Nat Rev Drug Discov* **14**, 499-509 (2015).

27. June CH, O'Connor RS, Kawalekar OU, Ghassemi S, Milone MC. CAR T cell immunotherapy for human cancer. *Science* **359**, 1361-1365 (2018).

28. Xiong W, *et al.* Immunological Synapse Predicts Effectiveness of Chimeric Antigen Receptor Cells. *Mol Ther* **26**, 963-975 (2018).

29. Basu R, *et al.* Cytotoxic T Cells Use Mechanical Force to Potentiate Target Cell Killing. *Cell* **165**, 100-110 (2016).

30. Yokosuka T, Takamatsu M, Kobayashi-Imanishi W, Hashimoto-Tane A, Azuma M, Saito T. Programmed cell death 1 forms negative costimulatory microclusters that directly inhibit T cell receptor signaling by recruiting phosphatase SHP2. *The Journal of Experimental Medicine* **209**, 1201 (2012).

31. Kim K, *et al.* Correlative three-dimensional fluorescence and refractive index tomography: bridging the gap between molecular specificity and quantitative bioimaging. *Biomed Opt Express* **8**, 5688-5697 (2017).

32. Shin S, Kim D, Kim K, Park Y. Super-resolution three-dimensional fluorescence and optical diffraction tomography of live cells using structured illumination generated by a digital micromirror device. *Sci Rep-Uk* **8**, 9183 (2018).

33. Chowdhury S, Eldridge WJ, Wax A, Izatt JA. Structured illumination microscopy for dual-modality 3D sub-diffraction resolution fluorescence and refractive-index reconstruction. *Biomed Opt Express* **8**, 5776-5793 (2017).